

1 An Improved Hydrometeor Detection Method for Millimeter-Wavelength Cloud

2 Radar

3 Jinming Ge¹, Zeen Zhu¹, Chuang Zheng¹, Hailing Xie¹, Tian Zhou¹, Jianping Huang¹,

4 and Qiang Fu^{1,2}

5 ¹Key Laboratory for Semi-Arid Climate Change of the Ministry of Education and

6 College of Atmospheric Sciences, Lanzhou University, Lanzhou, 730000, PRC

7 ²Department of Atmospheric Sciences, University of Washington, Seattle, WA,

8 98105, USA

9

10

11

12

13

14

15

16

17

18

19

20 Submitted to *Atmos. Chem. and Phys.*

21

July 3, 2017

Abstract

22

23 A modified method with a new noise reduction scheme that can reduce the noise
24 distribution to a narrow range is proposed to distinguish clouds and other hydrometeors
25 from noise and recognize more features with weak signal in cloud radar observations.
26 A spatial filter with central weighting, which is widely used in cloud radar hydrometeor
27 detection algorithms, is also applied in our method to examine radar return for
28 significant levels of signals. “Square clouds” were constructed to test our algorithm and
29 the method used for the U.S. Department of Energy Atmospheric Radiation
30 Measurements Program millimeter-wavelength cloud radar. We also applied both the
31 methods to six months of cloud radar observations at the Semi-Arid Climate and
32 Environment Observatory of Lanzhou University and compared the results. It was
33 found that our method has significant advantages in reducing the rates of both failed
34 negative and false positive hydrometeor identifications in simulated clouds and
35 recognizing clouds with weak signal from our cloud radar observations.

36 1. Introduction

37 Clouds, which are composed of liquid water droplets, ice crystals or both, cover
38 about two-thirds of the earth surface at any time [e.g., *King et al.*, 2013]. By reflecting
39 solar radiation back to the space (the albedo effect) and trapping thermal radiation
40 emitted by the Earth surface and the lower troposphere (the greenhouse effect), clouds
41 strongly modulate the radiative energy budget in the climate system [e.g., *Fu et al.*,
42 2002; *Huang et al.*, 2007; *Huang et al.*, 2006a; *Huang et al.*, 2006b; *Ramanathan et al.*,
43 1989; *Su et al.*, 2008]. Clouds are also a vital component of water cycle by connecting
44 the water-vapor condensation and precipitation. Despite the importance of clouds in the
45 climate system, they are difficult to represent in climate models [e.g., *Williams and*
46 *Webb*, 2009], which causes the largest uncertainty in the predictions of climate change
47 by general circulation models (GCMs) [e.g., *Randall*, 2007; *Stephens*, 2005; *Williams*
48 *and Webb*, 2009].

49 Cloud formation, evolution and distribution are governed by complex physical and
50 dynamical processes on a wide range of scales from synoptic motions to turbulence
51 [*Bony et al.*, 2015]. Unfortunately, the processes that occur on smaller spatial scales
52 than a GCM grid box cannot be resolved by current climate models, and the coupling
53 between large scale fluctuations and cloud microphysical processes are not well
54 understood [e.g., *Huang et al.*, 2006b; *Mace et al.*, 1998; *Yan et al.*, 2015; *Yuan et al.*,
55 2006]. Moreover, the cloud horizontal inhomogeneity and vertical overlap are not
56 resolved by GCMs [*Barker*, 2000; *Barker and Fu*, 2000; *Fu et al.*, 2000a; *Fu et al.*,
57 2000b; *Huang et al.*, 2005; *Li et al.*, 2015]. To better understand cloud processes for

58 improving their parameterization in climate models and revealing their evolution in
59 response to climate change, long-term continuous observations of cloud fields in terms
60 of both macro- and micro-physical properties are essential [e.g., *Ackerman and Stokes,*
61 *2003; Sassen and Benson, 2001; Thorsen et al., 2011; Wang and Sassen, 2001*].

62 Millimeter-wavelength Cloud Radars (MMCRs) can resolve cloud vertical structure
63 for their occurrences and microphysical properties [e.g., *Clothiaux et al., 1995; Kollias*
64 *et al., 2007a; Mace et al., 2001*]. The wavelengths of MMCRs are shorter than those of
65 weather radars making them sensitivity to cloud droplets and ice crystals and can
66 penetrate multiple cloud layers [e.g., *Kollias et al., 2007a*]. Because of their outstanding
67 advantages for cloud research, millimeter-wavelength radars have been deployed on
68 various research platforms including the first space-borne millimeter-wavelength Cloud
69 Profiling Radar (CPR) onboard the CloudSat [*Stephens et al., 2002*]. Ground-based
70 cloud radar are operated at the U.S. Department of Energy's Atmospheric Radiation
71 Program (ARM) observational sites (used to be MMCRs, now are replaced with a new
72 generation of Ka band Zenith Radar (KAZR)) [e.g., *Ackerman and Stokes, 2003;*
73 *Clothiaux et al., 2000; Clothiaux et al., 1999; Kollias et al., 2007b; Protat et al., 2011*]
74 and in Europe [*Illingworth et al., 2007; Protat et al., 2009*]. In July 2013, a KAZR was
75 deployed in China at the Semi-Arid Climate and Environment Observatory of Lanzhou
76 University (SACOL) site (latitude: 35.946°N; longitude: 104.137°E; altitude: 1.97 km)
77 [*Huang et al., 2008*], providing an opportunity to observe and reveal the detailed
78 structure and process of the mid-latitude clouds over the semi-arid regions of East Asia.

79 Before characterizing the cloud physical properties from the cloud radar return signal,

80 we first need to distinguish and extract the hydrometeor signals from the background
81 noise (i.e. cloud mask). A classical cloud mask method was developed in Clothiaux et
82 al.[2000; 1995] by analyzing the strength and significance of returned signals. This
83 method consists of two main steps. First any power in a range gate that is greater than
84 a mean value of noise plus one standard deviation is selected as a bin containing
85 potential hydrometer signal. Second, a spatial-time coherent filter is created to estimate
86 the significance level of the potential hydrometer bin signal to be real. This cloud mask
87 algorithm is operationally used for the ARM MMCRs data analysis and was later
88 adopted to the CPR onboard the CloudSat [*Marchand et al.*, 2008].

89 It is recognized that by visually examining a cloud radar return image, one can easily
90 tell where the return power is likely to be caused by hydrometeors and where the power
91 is just from noise. This ability of human eye on extracting and analyzing information
92 from an image has been broadly studied in image processing and computer vision. A
93 number of mathematical methods for acquiring and processing information from
94 images have been developed, including some novel algorithms for noise reduction and
95 edge detection [*Canny*, 1986; *He et al.*, 2013; *Marr and Hildreth*, 1980; *Perona and*
96 *Malik*, 1990]. In this paper, we propose a modified cloud mask method for cloud radar
97 by noticing that removing noise from signal and identifying cloud boundaries are the
98 essential goals of cloud mask. This method reduces the radar noise while preserving
99 cloud edges by employing the bilateral filtering that is widely used in the image
100 processing [*Tomasi and Manduchi*, 1998]. The power weighting probability method
101 proposed by Marchand et al.[2008] is also adopted in our method to prevent the cloud

102 corners from being removed. It is found that our improved hydrometeor detection
103 algorithm is efficient in terms of reducing false positives and negatives as well as
104 identifying cloud features with weak signals such as thin cirrus clouds.

105 The KAZR deployed at the SACOL is described in section 2 and the modified cloud
106 mask algorithm is introduced in section 3. The applications of the new scheme to both
107 hypothetical and observed cloud fields including a comparison with previous schemes
108 are shown in section 4. Summary and conclusions are given in section 5.

109 2. The KAZR Radar

110 The SACOL KAZR, built by ProSensing Inc. of Amherst, MA, is a zenith-pointing
111 cloud radar operating at approximately 35 GHz for the dual-polarization measurements
112 of Doppler spectra. The main purpose of the KAZR is to provide vertical profiles of
113 clouds by measuring the first three Doppler moments: reflectivity, radial Doppler
114 velocity, and spectra width. The linear depolarization ratio [*Marr and Hildreth*, 1980]
115 can be computed from the ratio of cross-polarized reflectivity to co-polarized
116 reflectivity.

117 The SACOL KAZR has a transmitter with a peak power of 2.2 kw and two modes
118 working at separate frequencies. One is called “chirp” mode that uses a linear-FM
119 (frequency modulation) pulse compression to achieve high radar sensitivity of about -
120 65 dBZ at 5 km altitude. The minimum altitude (or range) that can be detected in chirp
121 mode is approximately 1 km AGL. To view clouds below 1 km, a short pulse or “burst
122 mode” pulse is transmitted at a separate frequency just after transmission of the chirp
123 pulse. This burst mode pulse allows clouds as low as 200 m to be measured. The chirp

124 pulse is transmitted at 34.890 GHz while the burst pulse is transmitted at 34.830 GHz.

125 These two waveforms are separated in the receiver and processed separately.

126 The pulse length is approximately 300 ns (giving a range resolution of about 45 m),
127 while the digital receiver samples the return signal every 30 m. The interpulse period is
128 208.8 μ s, the number of coherent averages is 1, and the number of the fast Fourier
129 transform points is currently set to 512. An unambiguous range is thus 31.29 km, an
130 unambiguous velocity is 10.29 m/s, and a velocity resolution is 0.04m/s. The signal
131 dwell time is 4.27s. These operational parameters are set for the purpose of having
132 enough radar sensitivity and accurately acquiring reflectivities of hydrometeors. In this
133 study, we mainly use radar observed reflectivity (dBZ) data to test our new hydrometeor
134 detection method.

135 3. Improved hydrometeor detection algorithm

136 The basic assumption in the former cloud mask algorithms [e.g., *Clothiaux et al.*,
137 1995; *Marchand et al.*, 2008] is that the random noise power follows the normal
138 distribution. Here clear sky cases in all seasons from the KAZR observations were first
139 analyzed for its background noise power distributions. Figure 1a shows an example of
140 a clear-sky case during 0000 to 1200 UTC on January 21st, 2014. The noise power is
141 estimated from the top 30 range gates, which includes both internal and external
142 sources[*Fukao and Hamazu*, 2014]. It has an apparent non-Gaussian distribution with
143 a positive skewness of 1.40 (Fig.1a). The signal-to-noise ratio (SNR) is defined as:

$$144 \quad \text{SNR} = 10\log\left(\frac{P_s}{P_n}\right) \quad (1)$$

145 where P_s is the power received at each range gate in a profile, P_n is the mean noise

146 power that is estimated by averaging the return power in the top 30 range gates which
147 are between 16.8 and 17.7 km AGL. Since this layer is well above the tropopause, few
148 atmospheric hydrometeors existing in this layer can scatter enough power back to
149 achieve the radar sensitivity. Figure 1a shows that the SNRs for clear skies closely
150 follow a Gaussian distribution. Instead of using radar received power, the SNR is used
151 as the input in our cloud mask algorithm including estimating the background noise
152 level. This is because in our method the chance for a central range gate to be a noise or
153 a potential feature, relies on the probability for a given range of SNR values following
154 the Gaussian distribution. Note that the mean value of the SNR for the noise power is
155 not zero, but a small negative value of about -0.3. This is because the mean of the noise
156 power is larger than its the median due to its positive skewed distribution. It is further
157 noted that for the noise the distribution of SNR and its mean for the top 30 range gates
158 are the same as those from the lower atmosphere.

159 The SNR value is treated as the brightness of a pixel in an image $f(x,y)$ in our
160 hydrometeor detection method. In an image processing, the random noise can be
161 smoothed out by using a low pass filter, which gives a new value for a pixel of an image
162 by averaging with neighboring pixels [*Tomasi and Manduchi, 1998*]. The cloud signals
163 are highly correlated in both space and time and have more similar values in near pixels
164 while the random noise values are not correlated. Figure 2a shows a schematic
165 comparison of the original noise, reduced noise and hydrometeor signal distributions:
166 the low pass filter could efficiently reduce the original radar noise represented by the
167 green line to a narrow bandwidth (blue line) while keeping the signal preserved. By

168 reducing the standard deviations of noise, which shrinks the overlap region of signal
169 and noise and enhances their contrast, the weak signals (yellow area) that cannot be
170 detected based on original noise level may become distinguished.

171 Following this idea, we develop a non-iterative hydrometeor detection algorithm
172 by applying a noise reduction and a central pixel weighting schemes. Figure 3 shows
173 the schematic flow diagram of our method. For given mean SNR values (S_o) and one
174 standard deviation (σ_o) of the original background noise, the input SNR data set is first
175 separated into two groups. One group with values greater than $S_o + 3\sigma_o$ are
176 considered as the cloud features that can be confidently identified. Another group with
177 values between S_o and $S_o + 3\sigma_o$ may potentially contain moderate ($S_o + \sigma_o <$
178 $SNR \leq S_o + 3\sigma_o$) to weak ($S_o < SNR \leq S_o + \sigma_o$) cloud signals, which will further go
179 through a noise reduction process. Here S_o and σ_o are estimated from the top 30
180 range gates of each five successive profiles.

181 The noise reduction process is performed by convolving radar SNR time-height
182 data with a low pass filter. The Gaussian Filter, which outputs a 'weighted average' of
183 each pixel and its neighborhood with the average weighted more towards the value of
184 the central pixel (v_0), is one of the most common functions of the noise reduction filter.

185 A 2-D Gaussian distribution kernel, shown in Fig. 2b₁, can be expressed as:

$$186 \quad G(i, j) = \frac{1}{2\pi\sigma^2} \exp\left(-\frac{i^2+j^2}{2\sigma^2}\right) \quad (2)$$

187 where i and j are the indexes in a filter window which are 0 for the central pixel, and σ
188 is standard deviation of the Gaussian distribution for the window size of the kernel.

189 Equation (2) is used in our study to filter the radar SNR image. Note that the

190 convolution kernel is truncated at about three standard deviations away from the mean
191 in order to accurately represent the Gaussian distribution. Figure 1b are the cumulative
192 distribution functions (CDFs) of clear sky SNR by convolving the same data in Fig. 1a
193 with filters that have different kernel sizes (3×3 , 5×5 , 7×7 and 9×9 pixels)
194 corresponding to the σ ranging from 0.5 to 2. The original SNR values are distributed
195 from about -5 to 5. After convolving the image with the Gaussian filter, the SNR
196 distribution can be constrained to a much narrower range. It is clear that the filter with
197 a larger kernel size is more effective in suppressing the noise. Shown in Fig. 1c are
198 results for a cloudy case on January 4th,2014 by applying the filter to the range gates
199 inside the cloud but adjacent to the boundary. It is shown that a larger kernel size shifts
200 the SNR farther away from the noise region. It therefore appears that increasing the
201 standard deviation (i.e. the window size) would reduce the noise and enhance the
202 contrast between signal and noise more effectively. At the same time, however, a larger
203 kernel can also attenuate or blur the high frequency components of an image (e.g., the
204 boundary of clouds) more. As shown in Fig. 1d, when the window size is increased
205 from 3×3 ($\sigma=0.5$) to 9×9 ($\sigma=2$), the SNR distribution of the range gates that are outside
206 the cloud but adjacent to the boundary gradually move toward larger values. This will
207 consequently raise the risk of misidentifying cloud boundaries. To solve this problem,
208 a bilateral filtering idea proposed by *Tomasi and Manduchi* [1998] is adopted here.
209 Considering a sharp edge between cloudy and clear region as shown in Fig. 2b₂, we
210 define a $\delta(i, j)$ function that when the central pixel is on the cloudy or clear side, gives
211 a weighting of 1 to the similar neighboring pixels (i.e. on the same side), and 0 to the

212 other side. After combining this δ function to the Gaussian kernel in Fig. 2b₁, we can
 213 get a new non-linear function called bilateral kernel as shown in Fig. 2b₃. It can be
 214 written as:

$$215 \quad B(i, j) = \frac{1}{2\pi\sigma^2} \exp\left(-\frac{i^2+j^2}{2\sigma^2}\right) \cdot \delta(i, j). \quad (3)$$

216 Thus the bilateral kernel will reduce averaging noises with signals, and vice versa. The
 217 noise-reduced image $h(x, y)$ is produced by convolving the bilateral kernel with the
 218 original input image $f(x, y)$ as:

$$219 \quad h(x, y) = k^{-1}(x, y) \sum_{j=-w}^{j=w} \sum_{i=-w}^{i=w} f(x + i, y + j) \cdot B(i, j) \quad (4)$$

220 where $\pm w$ is the bounds of the finite filter window, $k^{-1}(x, y)$ is defined as
 221 $1 / \sum_{j=-w}^{j=w} \sum_{i=-w}^{i=w} B(i, j)$ which is used to normalize the weighting. Since the bilateral
 222 kernel function only average the central pixel with neighbors on the same side (Fig. 2b),
 223 ideally it will preserve sharp edges of a target. We will discuss how to construct the δ
 224 function in order to group the central pixel with its neighbors later in this section. In the
 225 noise reduction process, a 5×5 window size (i.e., 25 bins in total) is specified for the
 226 low pass filter, which is empirically determined by visually comparing the cloud masks
 227 with original images. We should keep in mind that a small window size is less effective
 228 in noise reduction but a large window is not suitable for recognizing weak signals.

229 For performing the noise reduction with Eq. (4) in a 5×5 filter window, the number
 230 of range bins (N_s) with signal greater than $S_o + 3\sigma_o$ are first counted. These N_s range
 231 bins are then subtracted from the total 25 of the range bins in the filter window. Note
 232 that a noise reduction is only applied when the central pixel is among the $25 - N_s$ bins,
 233 and the δ function is set to be zero for the N_s range bins. If the remaining $25 - N_s$ range

234 bins are all noises, the range bin number (N_m) with SNR greater than $S_o + \sigma_o$ should
 235 be about equal to an integral number (N_t) of $0.16 \times (25 - N_s)$ where 0.16 is the probability
 236 for a remaining range bin to have a value greater than $S_o + \sigma_o$ for a Gaussian noise.
 237 Thus when N_m is equal to or smaller than N_t , all the $25 - N_s$ range bins could only
 238 contain pure noise and/or some weak cloud signals. In this case, the δ function is set
 239 to 1 for all the $25 - N_s$ bins. When N_m is found to be larger than N_t , the $25 - N_s$ range
 240 bins might contain a combination of moderate signal, noise and/or some weak clouds.
 241 In this case, $S_o + \sigma_o$ is selected as a threshold to determine whether the pixels are on
 242 the same side of the central pixel. If the central pixel has a value greater than $S_o + \sigma_o$,
 243 the δ function is assigned to 1 for the $25 - N_s$ pixels with $SNR \geq S_o + \sigma_o$, but 0 for the
 244 bins with $SNR < S_o + \sigma_o$. If the central pixel is less than $S_o + \sigma_o$, the δ function is
 245 assigned to 1 for the pixels with $SNR < S_o + \sigma_o$, but 0 for the $25 - N_s$ bins with
 246 $SNR \geq S_o + \sigma_o$.

247 After picking out the strong return signals and applying the noise reduction scheme,
 248 the new background noise S_n and its standard deviation σ_n are estimated. While S_n is
 249 the same as S_o , the σ_n is significantly reduced, which is a half of σ_o . This will make
 250 it possible to identify more hydrometeors as exhibited in Fig.2a. We assign different
 251 confidence level value (which is called the mask value in this study) to the following
 252 initial cloud mask according to the SNR. 40 is first assigned to the mask of any range
 253 bins with $SNR > S_o + 3\sigma_o$ in the original input data. For the rest of the range bins
 254 after applying the noise reduction, if the $SNR > S_n + 3\sigma_n$, the mask is assigned to be
 255 30; if $S_n + 2\sigma_n < SNR \leq S_n + 3\sigma_n$, the mask is 20; if $S_n + \sigma_n < SNR \leq S_n + 2\sigma_n$,

256 the mask is 10; and the remaining range bin mask is assigned to be 0. Thus, a mask
257 value assigned to a pixel represents the confident level for the pixel to be a feature.

258 To reduce both false positives (i.e. false detections) and false negatives (i.e. failed
259 detections), the next step is to estimate whether a range gate contains significant
260 hydrometeor. Following Clothiaux et al.[2000; 1995] and Marchand et al.[2008], a 5×5
261 spatial filter is used to calculate the probability of clouds and noise occurring in the 25
262 range gates. The probability of central pixel weighting scheme proposed by Marchand
263 et al. [2008] is adopted here, and the weighting for the central pixel is assigned
264 according to its initial mask value. The probability is calculated by

$$265 \quad p = G(L)(0.16^{N_T})(0.84^{N_0}) \quad (5)$$

266 where N_0 is the number of masks with zero mask value, N_T is the number of masks
267 with non-zeros mask value and $N_0 + N_T = 25$; $G(L)$ is the weighting probability of
268 the central pixel that could be a false detection at a given significant level of L (i.e.,
269 mask value) in the initial cloud mask. Here $G(0)=0.84$, $G(10)=0.16$, $G(20)=0.028$, $G(\geq$
270 $30)=0.002$. If p estimated from Eq. (5) is less than a given threshold (p_{thresh}), then the
271 central pixel is likely to be a hydrometeor signal. The cloud mask value will be set to
272 the same value as in the initial mask if it is non-zero; otherwise it will be set to 10.
273 Likewise, if $p > p_{thresh}$, then the central pixel is likely to be noise and the mask value
274 will be set to 0. This process is iterated 5 times for each pixel to obtain the final cloud
275 mask.

276 Following Marchand et al. [2008] who well explained the logic of choosing a proper
277 threshold, p_{thresh} is calculated as

278
$$p_{thresh} = (0.16^{N_{thresh}})(0.84^{25-N_{thresh}}) \quad (6)$$

279 Note that a smaller p_{thresh} will keep the false positives lower but increase the false
 280 negative. Herein we adopt the p_{thresh} of 5.0×10^{-12} used in Clothiaux et al.[2000], which
 281 is approximately equivalent to $N_{thresh} = 13$.

282 Figure 4 illustrate the main steps of our detection method by using the data from
 283 January 8th, 2014. Figure 4a is the original SNR input. Figure 4b shows the SNR
 284 distribution after the noise reduction process. One can see that the SNR after being
 285 compressed to a narrow range, becomes much smoother than original input. This step
 286 significantly increases the contrast between signal and noise. Figure 4c indicates the
 287 range gates that potentially contain hydrometeors in the initial cloud mask. Figure 4d
 288 is the final result by applying the spatial filter.

289 4. Results

290 4.1 Detection test

291 To test the performance of our hydrometeor detection method, we create 7 squares
 292 of SNR with sides of 100, 50, 25, 15, 10, 5, and 3 bins to mimic the radar “time-height”
 293 observations as shown in Fig. 5. The background noise is randomly given by a Gaussian
 294 distribution with a mean S_0 and a standard deviation σ_0 . The targets in panels a₁, a₂
 295 and a₃ are set with different SNR values to represent situations in which clouds have
 296 strong, moderate and weak signals, respectively. In panel a₁, the targets signals are set
 297 to be $S_0 + 10\sigma_0$. In panel a₂, the targets signals distribute from $S_0 + \sigma_0$ to $S_0 + 3\sigma_0$
 298 with a mean value of $S_0 + 2\sigma_0$. In panel a₃, the targets SNRs range from S_0 to $S_0 +$
 299 σ_0 with a mean value of $S_0 + 0.5\sigma_0$.

300 The three middle panels in Fig. 5 show the results after applying the noise reduction.
301 Again, comparing with the input signals, we can see that the background noise is well
302 compressed and becomes smoother. The shapes of the square targets are all well
303 maintained with sharp boundaries for strong and moderate signals (see Fig.5 b1 and b2).
304 In Fig.5 b3 for weak signals, the 3-bin square target is not obvious while the other 6
305 squares are still distinguishable. To separate the compressed background noise from
306 hydrometeor signals, the 5×5 spatial filter is further applied to the noise-reduced data.
307 The three right panels in Fig.5 show the final mask results. Generally, the hydrometeor
308 detection method can identify those targets well. Six of the seven square targets can be
309 identified for clouds with strong and moderate SNR. The 3×3 square is missed because
310 the small targets cannot be resolved by the 5×5 spatial filter. Since the temporal
311 resolution of KAZR is about 4 seconds, we expect that a cloud only having 3 bins in
312 horizontal would be rare. For the targets with weak SNR values, the 3×3 and 5×5
313 square targets are missed, but the rest five square targets are successfully distinguished
314 and their boundaries are well maintained as shown in Fig.5 c3.

315 To further demonstrate the performance of our method for detecting the hypothetical
316 clouds in Fig.5 a1, a2, and a3, the false and failed detection rates are listed in the table
317 1. For strong signals, no background noise pixel is misidentified as one containing
318 hydrometeors at level 40. Although at levels less than 40, some noise pixels around the
319 edges of targets are identified as signals, the false detection is within 0.05%. The failed
320 detection rate is about 0.24%. For moderate signals, the failed detection rate is still as
321 small as 0.23%, while the false detection increases a little to 0.10% at the confidence

322 levels below 30. The failed detection can reach up to 9.77% for weak signal at level 10,
323 but more than 90% weak signals can be captured in our method. Note that the false
324 positive is less than 0.01%; in other words, any range gate that is detected likely as a
325 signal bin will have extremely high likelihood to contain hydrometeors although its
326 backscattered signal is weak.

327 The simple square clouds are also tested by using the ARM hydrometeor detection
328 algorithm developed for the MMCRs [*Clothiaux et al.*, 2000; 1995] which does not
329 include the noise reduction and weighting schemes. As can be seen in Fig. 6, this
330 algorithm can only find five of the seven square targets with strong and moderate SNR.
331 Meanwhile without central pixel weighting, the corners of the targets become rounded
332 and more than 2.23% of hydrometeors are missed for strong and moderate cloud cases.
333 More importantly, none of the weak cloud signals can be detected. Comparing Fig.5
334 and Fig.6, it is obvious that our hydrometeor detection method can well maintain the
335 cloud boundary, keep both false and failed detection rate as low as a few percent for
336 strong and moderate cloud cases, and has a remarkable advantage in recognizing weak
337 signals.

338 It is noted that the ARM program has recently developed a new operational cloud
339 mask algorithm for the KAZRs by applying the Hildebrand and Sekhon [1974]
340 technique to determine the SNR values along with the spatial filter (Karen Johnson,
341 personal communication, 2017). It is our future research task to compare our algorithm
342 with the ARM's new operational algorithm.

343 4.2 Application to the SACOL KAZR observations

344 Our hydrometeor detection method was then applied to the winter and summer
345 months (Dec. in 2013, Jan., Feb., Jun., Jul. and Aug. in 2014) KAZR data at the SACOL.
346 A micropulse lidar (MPL) transmitted at 527 nm is operated nearby the KAZR. Lidar
347 is more sensitive to thin cirrus clouds and thus used to assess the performance of our
348 algorithm. Figure 7 a, b & c show an one-day example of radar reflectivity, normalized
349 backscatter and depolarization ratio of lidar, respectively. The cloud masks from our
350 detection method and the ARM MMCR method are shown in Fig. 7d&e. The MPL
351 feature mask is derived by modifying the method developed in Thorsen et al. [2015]
352 and Thorsen and Fu [2015] (see Fig. 7f). The vertical and horizontal resolutions of the
353 radar and lidar are different, and we map the observed data and derived feature mask
354 on the same height and time coordinates for the purpose of a comparison. A distinct thin
355 feature layer appears at about 8 km during 1500 to 1830 UTC from the lidar observation
356 which is clearly identified as a cirrus cloud using the depolarization ratio. The contrast
357 between the cirrus layer and background from the KAZR observation (Fig. 7a) is very
358 weak, and only a few range gates are identified as the hydrometeors using the method
359 without the noise reduction and weighting (Fig. 7d). However, our cloud mask method
360 can find more range gates (about 2.8 times of ARM's result). All these increased range
361 bins from our method are also detected as thin cirrus by the MPL (Fig. 7f). Another
362 apparent discrepancy exists in the low atmosphere layer. A non-negligible number of
363 range gates at about 2 km are recognized as hydrometeor echoes by our method but
364 mostly missed by former technique. This feature layer is also apparent in lidar
365 observations with both relative large backscatter intensities and depolarization

366 ratios(Fig. 7b&c). MPL recognizes this feature as an aerosol layer. From our KAZR
367 observations, we did find some dust events that were detected by this millimeter
368 wavelength radar (see the auxiliary Fig.1). Those feature echoes detected by our method
369 might partly be caused by large dust particles. Although the dust is not desired for cloud
370 mask, the appearance of those particles dose prove the ability of our method on
371 recognizing weak signals.

372 The upper two panels in Fig. 8 compares the number of occurrences of the detected
373 hydrometeor range bins from our methods with that from the ARM MMCR algorithm
374 for the six months of data. Generally, one can see that the variations of the identified
375 hydrometeor numbers with height from the two techniques are in a good agreement.
376 The distinct discrepancies appear at about 2 km in Winter and above 13 km in Summer
377 where our method apparently identify more hydrometeors. To illustrate the
378 improvements of our method and quantitatively evaluate the two schemes used in the
379 algorithm, we plot the percent change of the detected hydrometeor bins form our
380 method comparing with that from the ARM MMCR method in the lower two panels in
381 Fig. 8. As expected from the results in the test square clouds, our method can identify
382 more signals. The remarkable feature is that the increased percentage is over 20% at
383 high altitude, indicating that our method can recognize more cirrus clouds. The
384 increased percentage of hydrometeor derived only with the weighting scheme (dashed
385 line) and with both the noise reduction and weighting schemes (solid line) are separated
386 to demonstrates the individual contribution of the scheme to the improvement of our
387 method. In winter, the number of the detected hydrometeors only with the weighting

388 scheme is almost the same as that from the ARM method at layer from 3.5 to 9 km
389 AGL, while this number will increase by about 5% if the noise reduction scheme is
390 involved, indicating that some hydrometeors with weak SNR values may exit in this
391 layer. Above and below this atmospheric layer, the increased percentage is largely
392 determined by the weighting scheme. In summer, the two lines almost overlap each
393 other between 3.5 and 9.5 km with values below 5%, revealing that the bins found by
394 our method in the middle atmospheric layer are mainly around the boundaries of clouds.
395 We may infer that in summer season, clouds in middle level are usually composed of
396 large droplets with strong SNR values. The two lines are gradually apart with height.
397 This is because hydrometeors in the upper troposphere usually have smaller size that
398 causes weak SNR values, which will be effectively detected by the noise reduction
399 scheme.

400 We also analyzed the data when both KAZR and MPL observations are available and
401 compared our KAZR cloud mask with MPL feature detection. Figure 9a shows the
402 percentage of the increased detections identified by both KAZR with our method and
403 MPL observations as normalized to the KAZR total increased detections. Here we
404 should point out that MPL has a difficulty to distinguish dust from clouds (especially
405 cirrus clouds). Unfortunately, there exist large amount of dust aerosols over the SACOL
406 region. We visually examined several cases and found many MPL signals, which
407 should be clouds, are misidentified as aerosols. For this reason, we compare the KAZR
408 increased detections with the features (i.e. cloud and aerosol) detected by MPL above
409 3 km. It is obviously that more than 90% of increased detections are also detected as

410 features by MPL. Below 3 km, we calculated the percentage by comparing the KAZR
411 detections only with the cloud pixels detected by MPL since aerosol is always present
412 in the lowest several kilometers. To test whether those increased detections, which are
413 not identified as cloud by MPL under 3 km, are signal or noise, we examined the PDFs
414 of MPL normalized aerosol backscatter and depolarization corresponding to the KAZR
415 increased feature and KAZR noise regions in Figure 10a & 10b. The PDFs of MPL
416 backscatter for the KAZR feature and noise regions are quite different (Fig.10a) with
417 the mean backscatter of 0.15 for feature and 0.10 (*photoelectrons km⁻²*)/($\mu\text{s } \mu\text{J}^{-1}$)
418 for noise. The mean of the MPL depolarization ratio is 0.16 for feature and 0.12 for
419 noise although the PDFs are similar (Fig.10b), because dust is the main aerosol type
420 over this region. We also plot the PDFs of KAZR SNR and LDR for the increased
421 feature and noise pixels (Figs. 10c and 10d). The PDFs of SNR and LDR are Gaussian-
422 like for noise pixels which are quite different from those for the increased detections.
423 Table 2 shows the mean values of the four quantities shown in Fig.10. All the
424 differences of these mean values between KAZR noise and increased feature regions
425 pass the significant test at 95% confidence level except for the MPL depolarization ratio.
426 These increased features from our feature mask could thus be dust (and/or some
427 plankton) but not be the false positive. Figure 9b shows the profile of false negative (i.e.
428 the percentage of the cloud pixels identified by MPL but not by KAZR in the total MPL
429 detected cloud pixels). We can see that our method with the noise reduction has relative
430 smaller false negatives especially in the layers under 3 km and between 7 and 10 km.
431 Table 3 is the confusion matrix of the KAZR feature mask results from both our and

432 the ARM MMCR methods estimated by MPL cloud feature. Overall, 70.7% cloud mask
433 identified by MPL also recognized by the new method, while this percent is 68.9% for
434 the algorithm without noise reduction. The difference of false positive between the two
435 methods is only 0.1% as shown in table 3. These numbers dose show an improvement
436 of our method on recognize weak signals by comparing with the results from the ARM
437 MMCR method, however, they can not be used to assess the accuracy of our method
438 due to the MPL feature detection issue.

439

440 5. Summary and Discussion

441 Based on image noise reduction technique, we propose a modified method to detect
442 hydrometeors from cloud radar return signals. The basic idea is to treat the SNR value
443 of each range gate as a pixel brightness and suppress the SNR distributions of noise to
444 a narrow range by convolving with a 2-D bilateral kernel which can effectively avoid
445 blurring the high frequency components (i.e. boundaries of a target). After the noise
446 smoothing process, a special filter with central-pixel weighting scheme is used to obtain
447 the final cloud mask. The detection of the test square clouds shows that there are two
448 remarkable advantages of our method. First the noise reduction scheme of our algorithm
449 can enhance the contrast between signal and noise, while keeping the cloud boundaries
450 preserved and detecting more hydrometeors with weak SNR values. Second both false
451 positive and failed negative rates for strong and moderate clouds can be reduced to
452 acceptably small values. A comparison of radar and lidar observations further highlight
453 the advantage of our method on recognizing weak cloud signal in application.

454

455 *Acknowledgements:* This work was supported by the National Science Foundation of
456 China (41430425, 41575016, 41521004, 41505011), China 111 project (No.B 13045),
457 and the Fundamental Research Funds for the Central University (lzujbky-2016-k01).

458 Reference

459 Ackerman, T. P., and G. M. Stokes (2003), The Atmospheric Radiation Measurement
460 program (vol 56, pg 38, 2003), *Physics Today*, 56(2), 14-14.

461 Barker, H. W. (2000), Indirect aerosol forcing by homogeneous and inhomogeneous
462 clouds, *Journal of Climate*, 13(22), 4042-4049, doi:10.1175/1520-
463 0442(2000)013<4042:iafbha>2.0.co;2.

464 Barker, H. W., and Q. Fu (2000), Assessment and optimization of the gamma-weighted
465 two-stream approximation, *Journal of the Atmospheric Sciences*, 57(8), 1181-1188,
466 doi:10.1175/1520-0469(2000)057<1181:aaootg>2.0.co;2.

467 Bony, S., et al. (2015), Clouds, circulation and climate sensitivity, *Nature Geoscience*,
468 8(4), 261-268, doi:10.1038/ngeo2398.

469 Canny, J. (1986), A COMPUTATIONAL APPROACH TO EDGE-DETECTION, *Ieee*
470 *Transactions on Pattern Analysis and Machine Intelligence*, 8(6), 679-698.

471 Clothiaux, E. E., T. P. Ackerman, G. G. Mace, K. P. Moran, R. T. Marchand, M. A.
472 Miller, and B. E. Martner (2000), Objective determination of cloud heights and radar
473 reflectivities using a combination of active remote sensors at the ARM CART sites,
474 *Journal of Applied Meteorology*, 39(5), 645-665, doi:10.1175/1520-
475 0450(2000)039<0645:odocha>2.0.co;2.

476 Clothiaux, E. E., M. A. Miller, B. A. Albrecht, T. P. Ackerman, J. Verlinde, D. M. Babb,
477 R. M. Peters, and W. J. Syrett (1995), AN EVALUATION OF A 94-GHZ RADAR FOR
478 REMOTE-SENSING OF CLOUD PROPERTIES, *Journal of Atmospheric and*
479 *Oceanic Technology*, 12(2), 201-229, doi:10.1175/1520-

480 0426(1995)012<0201:aeoagr>2.0.co;2.

481 Clothiaux, E. E., K. P. Moran, B. E. Martner, T. P. Ackerman, G. G. Mace, T. Uttal, J.
482 H. Mather, K. B. Widener, M. A. Miller, and D. J. Rodriguez (1999), The atmospheric
483 radiation measurement program cloud radars: Operational modes, *Journal of*
484 *Atmospheric and Oceanic Technology*, 16(7), 819-827, doi:10.1175/1520-
485 0426(1999)016<0819:tarmpc>2.0.co;2.

486 Fu, Q., M. Baker, and D. L. Hartmann (2002), Tropical cirrus and water vapor: an
487 effective Earth infrared iris feedback?, *Atmospheric Chemistry and Physics*, 2, 31-37.

488 Fu, Q., B. Carlin, and G. Mace (2000a), Cirrus horizontal inhomogeneity and OLR bias,
489 *Geophysical Research Letters*, 27(20), 3341-3344, doi:10.1029/2000gl011944.

490 Fu, Q., M. C. Cribb, and H. W. Barker (2000b), Cloud geometry effects on atmospheric
491 solar absorption, *Journal of the Atmospheric Sciences*, 57(8), 1156-1168.

492 Fukao, S., and K. Hamazu (2014), Radar for Meteorological and Atmospheric
493 Observations, *Springer*.

494 He, K., J. Sun, and X. Tang (2013), Guided Image Filtering, *Ieee Transactions on*
495 *Pattern Analysis and Machine Intelligence*, 35(6), 1397-1409,
496 doi:10.1109/tpami.2012.213.

497 Hildebrand, P. H., and R. S. Sekhon (1974), Objective Determination of the Noise Level
498 in Doppler Spectra *Journal of Applied Meteorology*, 13, 808~811, doi:
499 [http://dx.doi.org/10.1175/1520-0450\(1974\)013<0808:ODOTNL>2.0.CO;2](http://dx.doi.org/10.1175/1520-0450(1974)013<0808:ODOTNL>2.0.CO;2).

500 Huang, J. P., J. Ge, and F. Weng (2007), Detection of Asia dust storms using multisensor
501 satellite measurements, *Remote Sensing of Environment*, 110(2), 186-191,

502 doi:10.1016/j.rse.2007.02.022.

503 Huang, J. P., P. Minnis, B. Lin, Y. H. Yi, T. F. Fan, S. Sun-Mack, and J. K. Ayers (2006a),
504 Determination of ice water path in ice-over-water cloud systems using combined
505 MODIS and AMSR-E measurements, *Geophysical Research Letters*, 33(21),
506 doi:10.1029/2006gl027038.

507 Huang, J. P., P. Minnis, B. Lin, Y. H. Yi, M. M. Khaiyer, R. F. Arduini, A. Fan, and G.
508 G. Mace (2005), Advanced retrievals of multilayered cloud properties using
509 multispectral measurements, *Journal of Geophysical Research-Atmospheres*, 110(D15),
510 doi:10.1029/2004jd005101.

511 Huang, J. P., Y. J. Wang, T. H. Wang, and Y. H. Yi (2006b), Dusty cloud radiative forcing
512 derived from satellite data for middle latitude regions of East Asia, *Progress in Natural
513 Science*, 16(10), 1084-1089.

514 Huang, J. P., et al. (2008), An Overview of the Semi-arid Climate and Environment
515 Research Observatory over the Loess Plateau, *Advances in Atmospheric Sciences*, 25(6),
516 906-921, doi:10.1007/s00376-008-0906-7.

517 Illingworth, A. J., et al. (2007), Cloudnet - Continuous evaluation of cloud profiles in
518 seven operational models using ground-based observations, *Bulletin of the American
519 Meteorological Society*, 88(6), 883+, doi:10.1175/bams-88-6-883.

520 King, M. D., S. Platnick, W. P. Menzel, S. A. Ackerman, and P. A. Hubanks (2013),
521 Spatial and Temporal Distribution of Clouds Observed by MODIS Onboard the Terra
522 and Aqua Satellites, *Ieee Transactions on Geoscience and Remote Sensing*, 51(7), 3826-
523 3852, doi:10.1109/tgrs.2012.2227333.

524 Kollias, E. E. Clothiaux, M. A. Miller, B. A. Albrecht, G. L. Stephens, and T. P.
525 Ackerman (2007a), Millimeter-wavelength radars - New frontier in atmospheric cloud
526 and precipitation research, *Bulletin of the American Meteorological Society*, 88(10),
527 1608+, doi:10.1175/bams-88-10-1608.

528 Kollias, E. E. Clothiaux, M. A. Miller, E. P. Luke, K. L. Johnson, K. P. Moran, K. B.
529 Widener, and B. A. Albrecht (2007b), The Atmospheric Radiation Measurement
530 Program cloud profiling radars: Second-generation sampling strategies, processing, and
531 cloud data products, *Journal of Atmospheric and Oceanic Technology*, 24(7), 1199-
532 1214, doi:10.1175/jtech2033.1.

533 Li, J., J. Huang, K. Stamnes, T. Wang, Q. Lv, and H. Jin (2015), A global survey of
534 cloud overlap based on CALIPSO and CloudSat measurements, *Atmospheric
535 Chemistry and Physics*, 15(1), 519-536, doi:10.5194/acp-15-519-2015.

536 Mace, G. G., T. P. Ackerman, P. Minnis, and D. F. Young (1998), Cirrus layer
537 microphysical properties derived from surface-based millimeter radar and infrared
538 interferometer data, *Journal of Geophysical Research-Atmospheres*, 103(D18), 23207-
539 23216, doi:10.1029/98jd02117.

540 Mace, G. G., E. E. Clothiaux, and T. P. Ackerman (2001), The composite characteristics
541 of cirrus clouds: Bulk properties revealed by one year of continuous cloud radar data,
542 *Journal of Climate*, 14(10), 2185-2203, doi:10.1175/1520-
543 0442(2001)014<2185:tccocc>2.0.co;2.

544 Marchand, R., G. G. Mace, T. Ackerman, and G. Stephens (2008), Hydrometeor
545 detection using Cloudsat - An earth-orbiting 94-GHz cloud radar, *Journal of*

546 *Atmospheric and Oceanic Technology*, 25(4), 519-533, doi:10.1175/2007jtecha1006.1.

547 Marr, D., and E. Hildreth (1980), THEORY OF EDGE-DETECTION, *Proceedings of*
548 *the Royal Society Series B-Biological Sciences*, 207(1167), 187-217,
549 doi:10.1098/rspb.1980.0020.

550 Perona, P., and J. Malik (1990), SCALE-SPACE AND EDGE-DETECTION USING
551 ANISOTROPIC DIFFUSION, *Ieee Transactions on Pattern Analysis and Machine*
552 *Intelligence*, 12(7), 629-639, doi:10.1109/34.56205.

553 Protat, A., D. Bouniol, J. Delanoe, P. T. May, A. Plana-Fattori, A. Hasson, E. O'Connor,
554 U. Goersdorf, and A. J. Heymsfield (2009), Assessment of Cloudsat Reflectivity
555 Measurements and Ice Cloud Properties Using Ground-Based and Airborne Cloud
556 Radar Observations, *Journal of Atmospheric and Oceanic Technology*, 26(9), 1717-
557 1741, doi:10.1175/2009jtecha1246.1.

558 Protat, A., J. Delanoe, P. T. May, J. Haynes, C. Jakob, E. O'Connor, M. Pope, and M. C.
559 Wheeler (2011), The variability of tropical ice cloud properties as a function of the
560 large-scale context from ground-based radar-lidar observations over Darwin, Australia,
561 *Atmospheric Chemistry and Physics*, 11(16), 8363-8384, doi:10.5194/acp-11-8363-
562 2011.

563 Ramanathan, V., R. D. Cess, E. F. Harrison, P. Minnis, B. R. Barkstrom, E. Ahmad, and
564 D. Hartmann (1989), CLOUD-RADIATIVE FORCING AND CLIMATE - RESULTS
565 FROM THE EARTH RADIATION BUDGET EXPERIMENT, *Science*, 243(4887), 57-
566 63, doi:10.1126/science.243.4887.57.

567 Randall, D. A., R.A. Wood, S. Bony, R. Colman, T. Fichefet, J. Fyfe, V. Kattsov, A.

568 Pitman, J. Shukla, J. Srinivasan, R.J. Stouffer, A. Sumi and K.E. Taylor (2007), Climate
569 Models and Their Evaluation. In: Climate Change 2007: The Physical Science Basis,
570 *Contribution of Working Group I to the Fourth Assessment Report of the*
571 *Intergovernmental Panel on Climate Change, [Solomon, S., D. Qin, M. Manning, Z.*
572 *Chen, M. Marquis, K.B. Averyt, M.Tignor and H.L. Miller (eds.)]. Cambridge*
573 *University Press, Cambridge, United Kingdom and New York, NY, USA.*

574 Sassen, K., and S. Benson (2001), A midlatitude cirrus cloud climatology from the
575 facility for atmospheric remote sensing. Part II: Microphysical properties derived from
576 lidar depolarization, *Journal of the Atmospheric Sciences*, 58(15), 2103-2112,
577 doi:10.1175/1520-0469(2001)058<2103:amcccf>2.0.co;2.

578 Stephens, G. L. (2005), Cloud feedbacks in the climate system: A critical review,
579 *Journal of Climate*, 18(2), 237-273, doi:10.1175/jcli-3243.1.

580 Stephens, G. L., et al. (2002), The cloudsat mission and the a-train - A new dimension
581 of space-based observations of clouds and precipitation, *Bulletin of the American*
582 *Meteorological Society*, 83(12), 1771-1790, doi:10.1175/bams-83-12-1771.

583 Su, J., J. Huang, Q. Fu, P. Minnis, J. Ge, and J. Bi (2008), Estimation of Asian dust
584 aerosol effect on cloud radiation forcing using Fu-Liou radiative model and CERES
585 measurements, *Atmospheric Chemistry and Physics*, 8(10), 2763-2771.

586 Thorsen, and Q. Fu (2015), Automated Retrieval of Cloud and Aerosol Properties from
587 the ARM Raman Lidar. Part II: Extinction, *Journal of Atmospheric and Oceanic*
588 *Technology*, 32(11), 1999-2023, doi:10.1175/jtech-d-14-00178.1.

589 Thorsen, Q. Fu, and J. Comstock (2011), Comparison of the CALIPSO satellite and

590 ground-based observations of cirrus clouds at the ARM TWP sites, *Journal of*
591 *Geophysical Research-Atmospheres*, 116, doi:10.1029/2011jd015970.

592 Thorsen; Fu, Q. N., Rob K.; Turner David D.; Comstock Jennifer M. (2015), Automated
593 Retrieval of Cloud and Aerosol Properties from the ARM Raman Lidar. Part I: Feature
594 Detection, *JOURNAL OF ATMOSPHERIC AND OCEANIC TECHNOLOGY*, 32(11),
595 1977-1998, doi:10.1175/JTECH-D-14-00150.1.

596 Tomasi, C., and R. Manduchi (1998), Bilateral Filtering for Gray and Color Images,
597 *IEEE International Conference on Computer Vision, Bombay, India*,
598 doi:10.1109/ICCV.1998.710815.

599 Wang, Z., and K. Sassen (2001), Cloud type and macrophysical property retrieval using
600 multiple remote sensors, *Journal of Applied Meteorology*, 40(10), 1665-1682,
601 doi:10.1175/1520-0450(2001)040<1665:ctampr>2.0.co;2.

602 Williams, K. D., and M. J. Webb (2009), A quantitative performance assessment of
603 cloud regimes in climate models, *Climate Dynamics*, 33(1), 141-157,
604 doi:10.1007/s00382-008-0443-1.

605 Yan, H. R., J. P. Huang, P. Minnis, Y. H. Yi, S. Sun-Mack, T. H. Wang, and T. Y.
606 Nakajima (2015), Comparison of CERES-MODIS cloud microphysical properties with
607 surface observations over Loess Plateau, *Journal of Quantitative Spectroscopy &*
608 *Radiative Transfer*, 153, 65-76, doi:10.1016/j.jqsrt.2014.09.009.

609 Yuan, J., Q. Fu, and N. McFarlane (2006), Tests and improvements of GCM cloud
610 parameterizations using the CCCMA SCM with the SHEBA data set, *Atmospheric*
611 *Research*, 82(1-2), 222-238, doi:10.1016/j.atmosres.2005.10.009.

Cloud Type	Performance (%)	Cloud Mask Confidence Level			
		≥ 10	≥ 20	≥ 30	≥ 40
Strong	False positive	0.048	0.044	0.009	0
	Failed negative	0.244	0.244	0.244	0.244
Moderate	False positive	0.103	0.103	0.063	0
	Failed negative	0.229	0.229	0.229	100
Weak	False positive	0.007	0.006	0.003	0
	Failed negative	9.774	96.788	100	100

612 Table 1. Summary of false positives and failed negatives for hypothetical strong,
613 moderate and weak cloud cases in Fig.5 a1, a2, and a3, respectively.

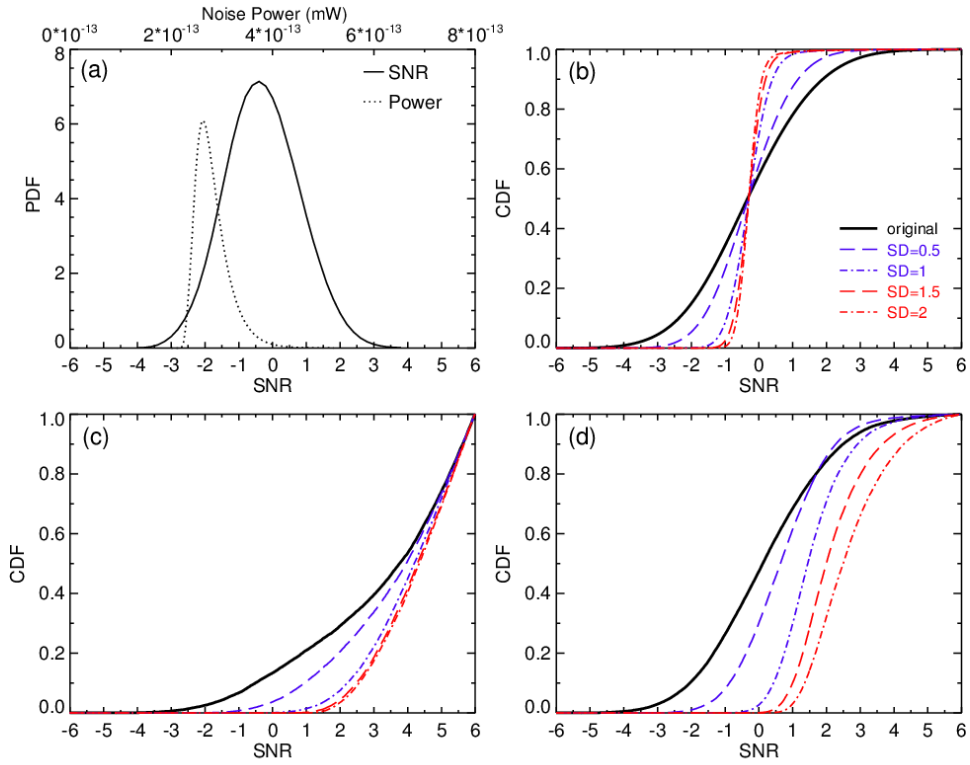
	increased KAZR feature	KAZA noise
MPL backscatter	0.15	0.10
MPL depolarization ratio	0.16	0.12
KAZR SNR	3.9	0.1
KAZR LDR	-3.0	-0.4

614 Table 2. Mean values of four quantities for KAZR increased feature and noise pixels

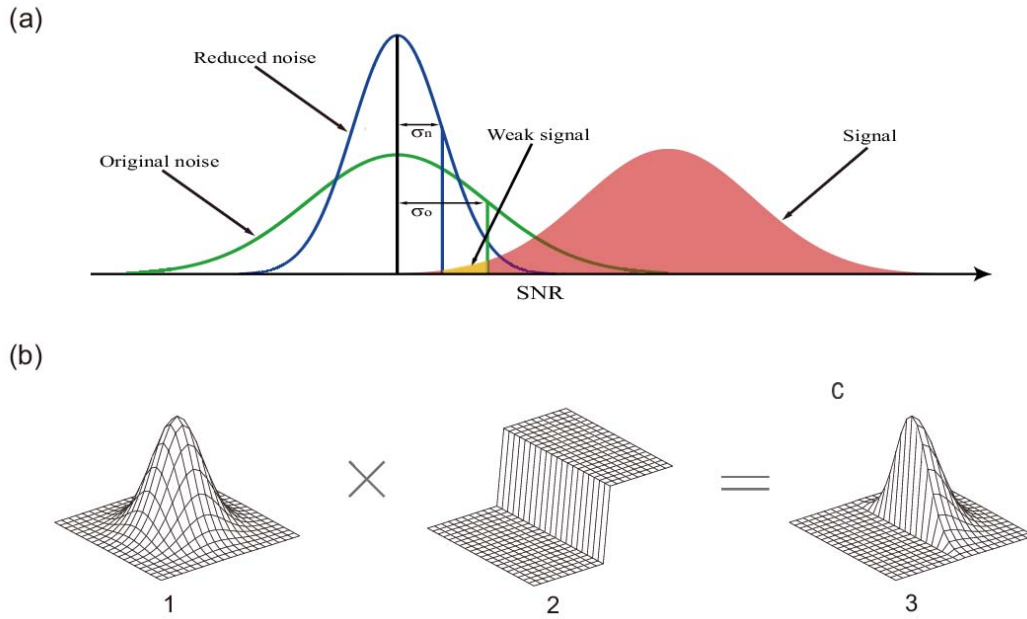
	our method	MMCR method
True Positive	70.7%	68.9%
True Negative	95.4%	95.5%
False Positive	4.6%	4.5%
False Negative	29.3%	31.1%

615 Table 3. Confusion matrix of KAZR mask results from our method and the ARM

616 MMCR algorithm estimated by MPL observations.

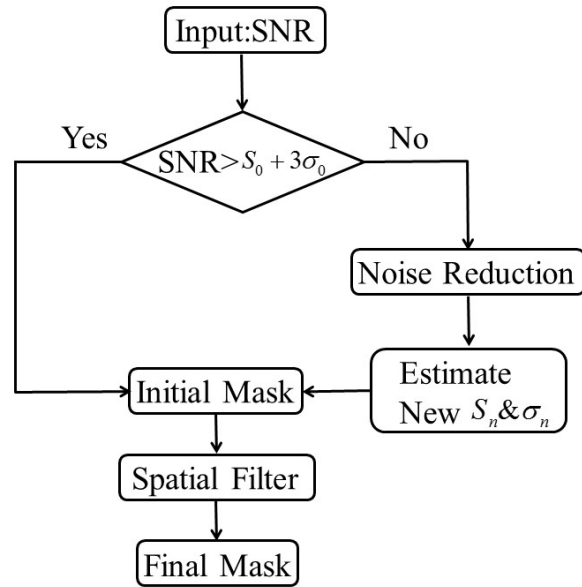


617 Figure 1. (a) Probability distribution function (PDF) of the noise power and SNR from
 618 the KAZR observations in a clear day of January 21, 2014. (b) Cumulative distribution
 619 function (CDF) of original and convolved SNR for the noise from the clear day. (c) and
 620 (d) CDF of original and convolved SNR from a cloudy case of January 4, 2014 for
 621 range gates inside and outside the cloud adjacent to the cloud boundary, respectively.
 622 The converted SNR is obtained by using a 2-D Gaussian distribution kernel (Eq. 2).

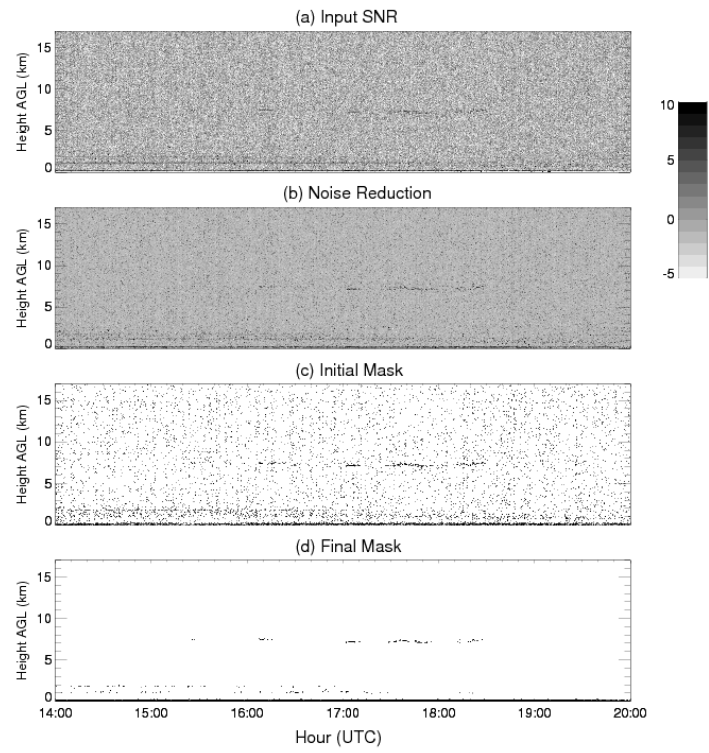


623 Figure 2. (a) comparison of original noise, reduced noise and hydrometeor signal
 624 distributions. σ_o and σ_n are one standard deviation of the original and reduced
 625 background noise, respectively. (b) Illustration of the bilateral filtering process. (b1)
 626 Gaussian kernel distribution in space. (b2) δ function. (b3) Bilateral kernel by
 627 combining Gaussian kernel with δ function.

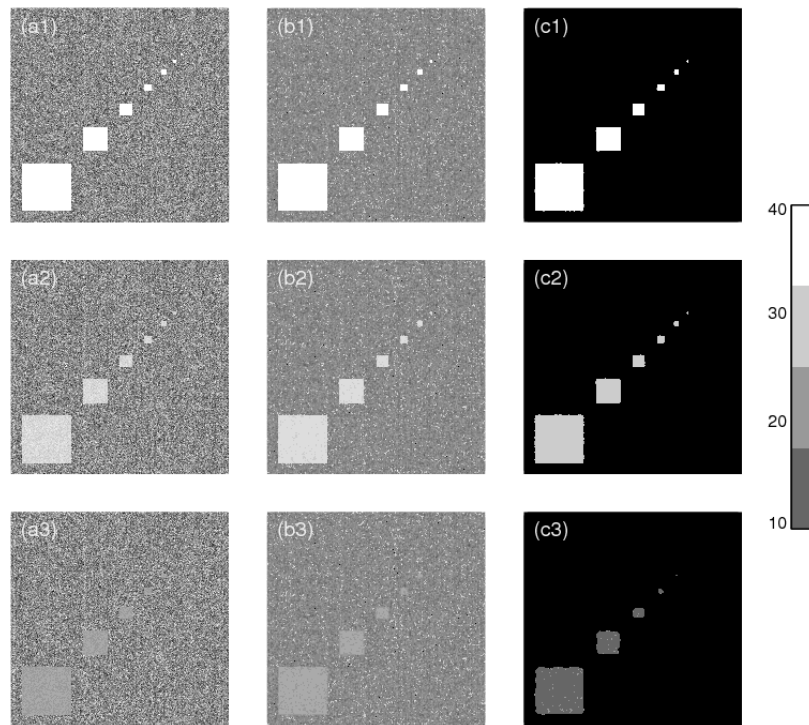
628



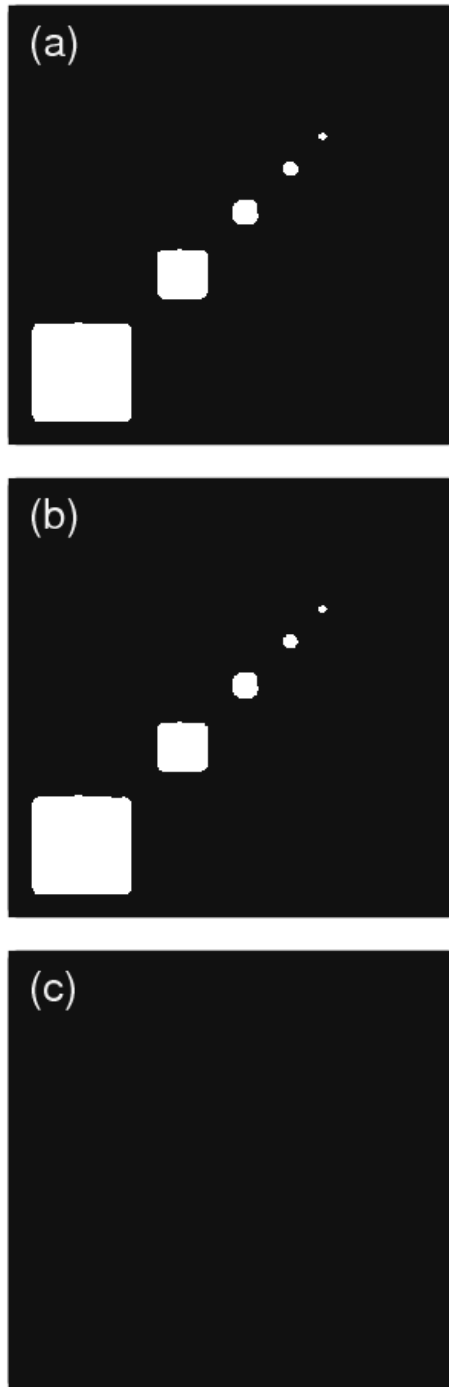
629 Figure 3. Schematic flow diagram for hydrometeor detection method. S_0 and S_n are
 630 the mean SNR for the original and reduced noise, respectively.



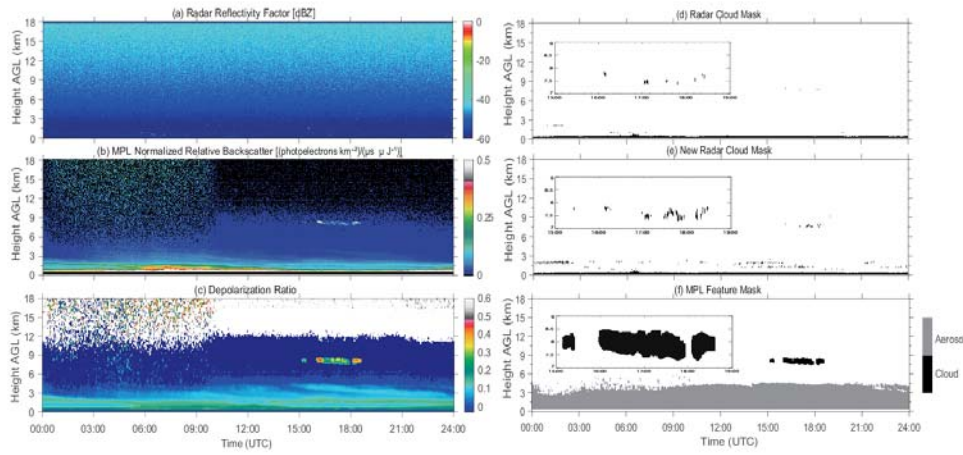
631 Figure 4. Illustration of the steps of the detection method using the real data of January
 632 8th, 2014.



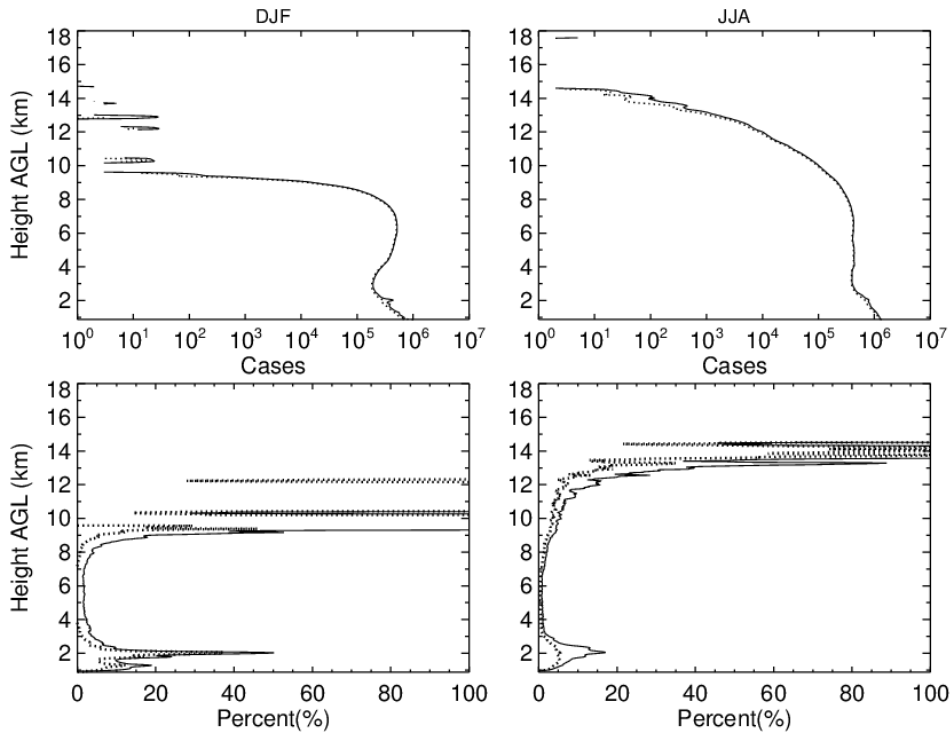
633 Figure 5. Panels a₁, a₂ and a₃ are three “square clouds” that have strong, moderate and
 634 weak SNR values with random Gaussian noise used to test the detection method. Panels
 635 b₁, b₂ and b₃ are SNR distributions after convolving the data with a bilateral kernel.
 636 Panels c₁, c₂ and c₃ are the final cloud mask filtered by the spatial filter.



637 Figure 6. Cloud mask without applying noise reduction and central pixel weighting. (a),
638 (b), (c) are for the targets with strong, moderate and weak SNR, respectively, from Fig.
639 4 a1, a2, and a3.

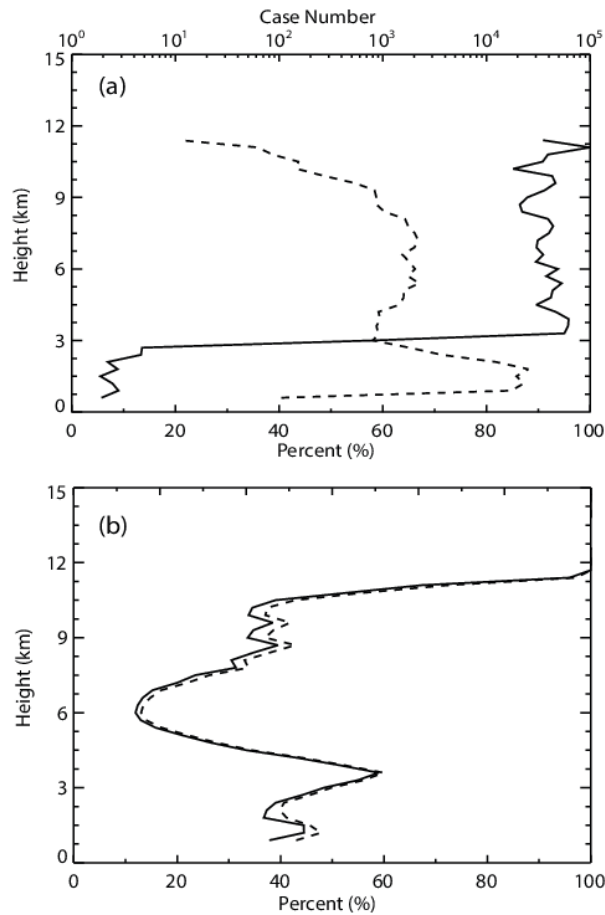


640 Figure 7. One-day example of radar- and lidar-observed cirrus cloud at the SACOL on
 641 January 8, 2014. (a) KAZR reflectivity. (b) MPL normalized backscatter intensity
 642 (c)MPL Depolarization Ration (d) radar cloud mask derived by the ARM MMCR
 643 algorithm. (e) radar cloud mask derived by our new method. (f) MPL feature mask.
 644 Three windows in (d), (e), (f) show the zoom-in views of cirrus masks.

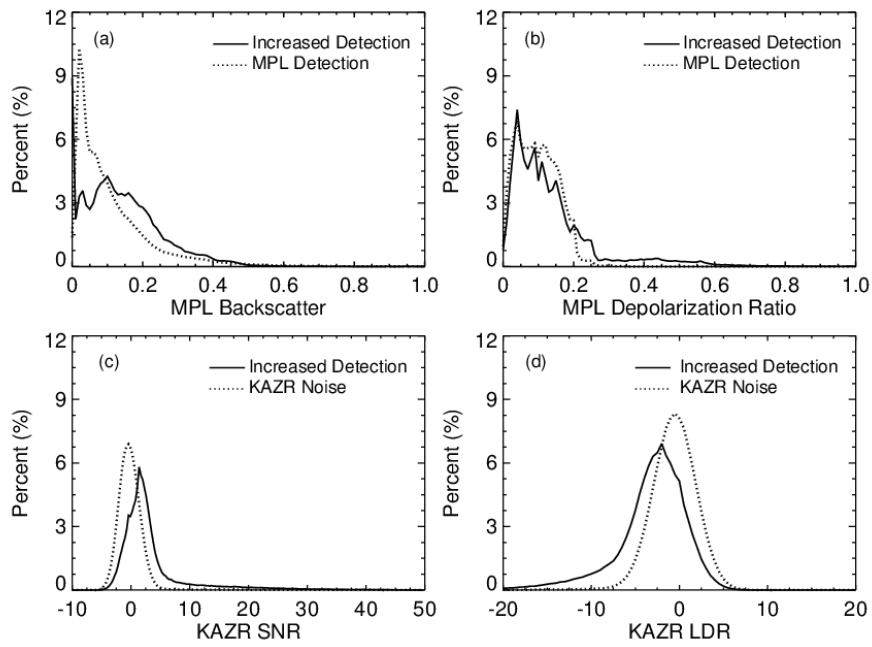


645 Figure 8. The upper panel shows the number of occurrences of the detected
 646 hydrometeor range bins from the two methods. The solid line is the number of range
 647 gates derived from our method. The dot line from the ARM MMCR algorithm. The
 648 lower two panels demonstrate the increased percentage of hydrometeor bins from our
 649 method comparing to the ARM MMCR algorithm. The solid line is calculated by
 650 applying both noise reduction and central-pixel weighting schemes, while the dashed
 651 line is calculated by only applying the central-pixel weighting scheme in our detection
 652 method.

653

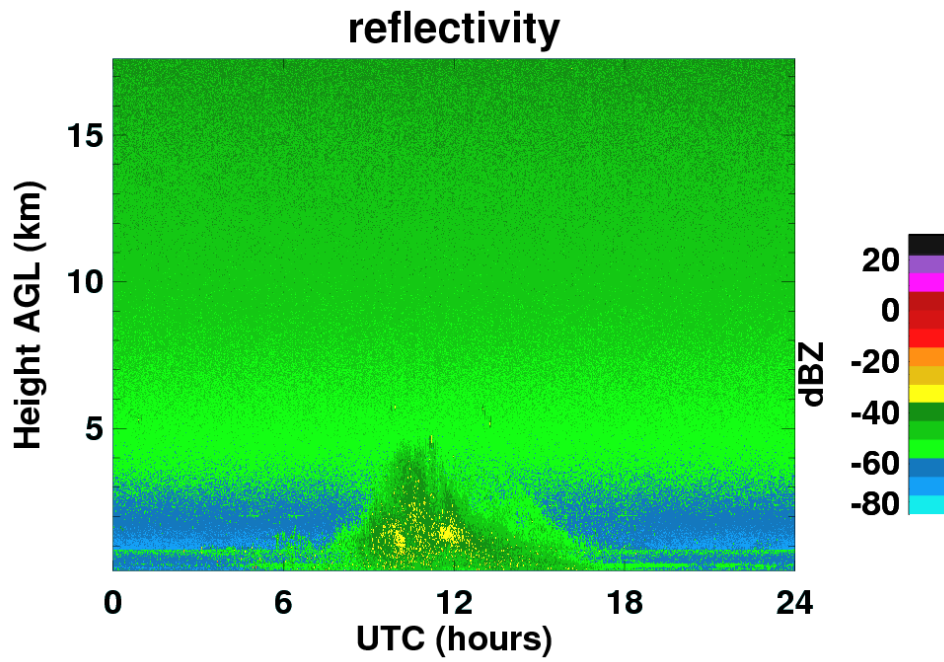


654 Figure 9. (a) A comparison of the increased detections with the MPL observations. (b)
 655 The percentage of the cloud pixels identified by MPL but not by KAZR in the total
 656 MPL detected cloud pixels. The solid line in Fig.9a is the percentage of increased
 657 detections seen by both KAZR with our method and MPL as compared with the total
 658 increased detections. The dash line in Fig.9a is the number of increased detections. The
 659 solid lines in Fig. 9b represents for the algorithm with noise reduction step. The dash
 660 line in Fig. 9b is for the method without noise reduction scheme.



661 Figure 10. PDF of (a) MPL Backscatter, (b) MPL depolarization Ratio, (c) KAZR SNR
 662 and (d) KAZR LDR for the KAZR increased detections (solid line) and KAZR noise
 663 (dashed line) pixels.

664



665 Auxiliary Figure 1. KAZR reflectivity on January 29th, 2014 at the SACOL, indicating
666 a dust event. The morphology and power level of the return signal is apparent not for a
667 cloud from the surface to the height of 5 km between 0800 to 1600 UTC.